

Start-to-end commissioning simulation for the HALF storage ring*

Ke-Min Chen,¹ Zhe Wang,¹ Tao He,¹ Duo-Hui He,¹ and Wei Xu^{1,†}

¹National Synchrotron Radiation Laboratory, University of Science and Technology of China, Hefei 230026, China

Hefei advanced light facility (HALF) is a 4th-generation diffraction-limited light source which started construction in 2023. The storage ring has an energy of 2.2 GeV and an extremely low emittance of less than 100 pm · rad. It contains 20 superperiods of the modified hybrid 6-bend achromat with a circumference of about 480 m. In reality, the real storage ring is different from the ideal lattice due to various kinds of errors. Those errors come from many sources, e.g., misalignment of components, imperfect magnetic fields, RF cavities, etc. Due to the small dynamic aperture and strong nonlinear effects, the errors have a serious effect on the 4th-generation storage ring, which brings great difficulties to its commissioning. To figure out the practical performance of the lattice with those errors, a start-to-end commission simulation is performed in this study, which also helps to verify the effectiveness of the commissioning of the HALF storage ring. In addition, the commissioning simulation process provides the basis for the development of the commissioning software for the HALF storage ring. Details and results of the commissioning simulation are reported in the paper.

Keywords: HALF, Storage ring, Commissioning simulation, Beam-based alignment, LOCO.

I. INTRODUCTION

The synchrotron radiation source has many properties such as high intensity, high brightness, transverse coherence, good time structure, very broad and continuous spectral range, etc [1, 2]. Since the 1970s, dedicated synchrotron radiation light sources have been developed as one of the most powerful scientific research tools over decades [3, 4]. The 4th-generation synchrotron radiation light source is proposed in recent years [5, 6]. By reducing the emittance of the electron beam in the storage ring, the brightness and coherence of the diffraction-limited synchrotron radiation are increased by two to three orders of magnitude compared with the 3rd-generation light sources [7, 8]. This huge and qualitative leap will greatly enhance the research capacity of synchrotron radiation, making it better to apply to the basic and applied researches. At present, there are several 4th-generation synchrotron radiation light sources that are already built, under construction, built or planned for upgrade in the world [9–13].

The Hefei advanced light facility (HALF) is a 4th-generation light source, which is under construction in Hefei, China [14]. The HALF storage ring contains 20 superperiods with modified hybrid 6-bend achromat with an emittance of less than 100 pm · rad. The goal of the HALF project is to build a high-performance synchrotron radiation light source in the VUV to soft X-ray region.

In a 4th-generation light source storage ring, the quadrupoles with strong strengths are used in order to obtain a low emittance, which results in the large negative chromaticities. To correct the chromaticities, intense sextupoles are adopted, leading to strong nonlinearity. Because of the strong quadrupoles and sextupoles, the magnetic field feed-down effects of the off-axis beam are large. Therefore, the errors of the machine components can severely affect the linear

optics and dynamic performance of the storage ring. Besides, the dynamic aperture of the ultra-low emittance storage ring is much smaller than that of the 3rd-generation ring, which causes additional difficulties to its commissioning. In order to figure out the performance of the storage ring and verify the effectiveness of the correction to various errors, a start-to-end simulated commissioning is essential. The simulated correction process is also the basis for the online commissioning of the HALF storage ring in the future. A recently developed Commissioning Simulation toolkit (SC) [15–19] based on the commonly used Accelerator Toolbox (AT) [20, 21] is adopted in this study.

The subsequent sections of this paper are organized as follows. In Sect. II, the basic performance and layout of the HALF storage ring are introduced. In Sect. III, settings of various errors are given. The performance of the storage ring without any correction is shown in Sect. IV. In Sect. V, the correction chain of the simulated commissioning process is shown. Finally, the summary and conclusion are given in Sect. VI.

II. THE HALF STORAGE RING

A. Lattice

The modified hybrid 6-bend achromat lattice structure is adopted by the HALF storage ring in order to obtain an ultra-low emittance [22, 23]. The natural emittance is 85.8 pm · rad with an energy of 2.2 GeV. The ring is composed of 20 identical cells which provides 20 long and 20 short straight sections. The optic functions and layout of the lattice is shown in Fig. 1. The unit cell contains 6 dipoles, 4 reverse bends, 16 quadrupoles, 8 sextupoles and 2 octupoles. All dipole magnets are longitudinal gradient bending (LGB) magnets which help to reduce the nature emittance along with the reverse bends. The quadrupoles are powered independently in order to tune the optic functions. The sextupoles are used to correct the chromaticities and optimize the dynamic performance. To save space, the slow orbit correctors

* Supported by the National Natural Science Foundation of China (No.11975227)

† Corresponding author, wxu@ustc.edu.cn

71 and skew quadrupole components are combined to those sex-
72 touples. The main parameters of the HALF storage ring are
73 shown in Table 1.

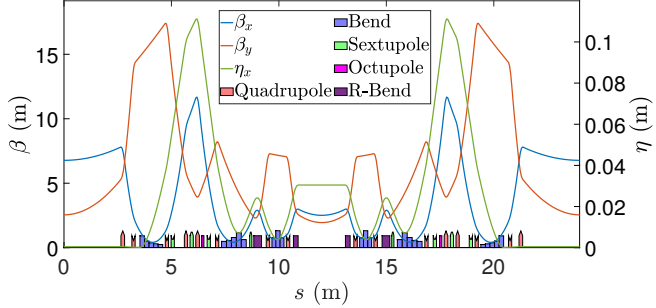


Fig. 1. (Color online) Optic functions of the HALF storage ring in one unit cell.

Table 1. Main parameters of the HALF storage ring.

Parameter	Value	Unit
Energy	2.2	GeV
Circumference	479.86	m
RF frequency	499.8	MHz
Harmonic number	800	-
Natural emittance	85.8	pm · rad
Transverse tunes	48.19/17.19	-
Natural Chromaticities	-81.6/-56.6	-
Corrected Chromaticities	+3/+3	-
Momentum compaction factor	9.4×10^{-5}	-
Damping partition number	1.36/1.00/1.64	-
Damping time	28.5/38.8/23.7	ms
Bunch length	1.32	mm
Natural energy spread	0.61×10^{-3}	-
Energy loss per turn	181.4	KeV
Synchrotron frequency	2.06	kHz
Linear energy acceptance	8.14	%

B. Dynamic performance

74 The HALF storage ring is carefully designed to optimize
75 its dynamic performance. The on-momentum 4D and 6D dy-
76 namic apertures (DA) of the HALF storage ring are shown in
77 Fig. 2, which are about 13 mm and 8 mm in the horizontal
78 plane respectively. Benefiting from the relatively large DA,
79 the off-axis injection scheme can be adopted, while it still
80 causes difficulties to the ring commissioning. The local mo-
81 mentum aperture (LMA) is shown in Fig. 3, which is obtained
82 by 6D tracking.

74

C. Monitors and correctors configuration

85 The configuration of the correctors and the beam position
86 monitors (BPMs) is shown in Fig. 4. Each cell contains 12
87 horizontal and vertical orbit correctors and 12 BPMs. Among

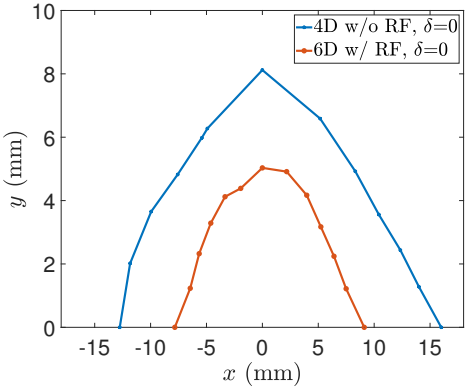


Fig. 2. (Color online) On-momentum dynamic aperture of the HALF storage ring.

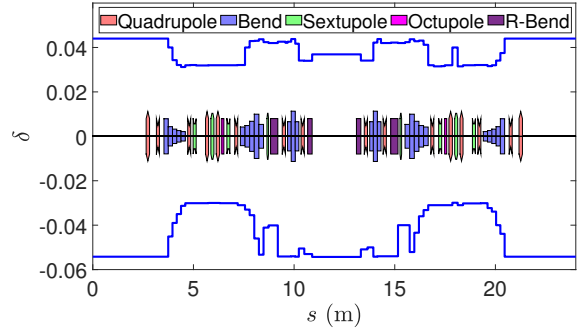


Fig. 3. (Color online) Local momentum aperture of the HALF stor-
age ring.

88 those correctors, 8 are combined to the multi-function sex-
89 touples, and 4 isolated correctors are located at the ends of the
90 straight sections. Skew quadrupole coils are combined to the
91 sextupole families SD1, SD2 and SF1 in order to correct the
92 coupling induced by the misalignment of the magnets. Since
93 the main vacuum chamber is a circular one with a diameter of
94 26 mm, a physical aperture with a radius of 13 mm is set to
95 all elements.

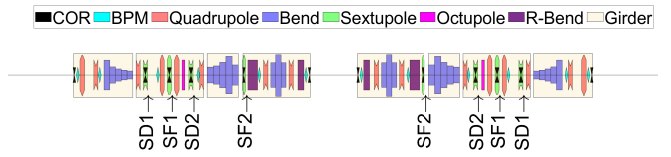


Fig. 4. (Color online) The configuration of correctors and BPMs in one unit cell.

96

III. ERROR SETTINGS

97 Before the commissioning simulation process, we need to
98 incorporate various types of errors into the lattice to imitate
99 the real machine. The random errors are generated based on

100 a 2σ -truncated Gaussian distribution, where σ represents the
 101 root mean square (RMS) of the errors.

102 A. Misalignment and magnetic field errors

103 The misalignment and field errors of the main magnets
 104 are detailed in Table 2. In a real machine, magnets are in-
 105 stalled on the girders. The magnets have misalignment errors
 106 while the girders also have misalignment errors. Therefore,
 107 the overall misalignment of the magnets are the sum of their
 108 own errors combined with the girder errors. The fields of the
 109 bends and quadrupoles are set with a 5×10^{-4} RMS frac-
 110 tional error. And the field errors of other multipoles are set to
 111 1×10^{-3} .

112 B. BPMs and correctors

113 The resolution of the BPM turn by turn (TBT) data is set
 114 to $1 \mu\text{m}$, and the resolution for the closed orbit slow acquisi-
 115 tion (SA) data is set to $0.1 \mu\text{m}$. A calibration error of the sum
 116 signal of 3% is assumed. The maximum strength of the orbit
 117 correctors is 1 mrad in both horizontal and vertical planes.
 118 To correct the ring coupling, skew quadrupoles with a max-
 119 imum strength of 0.27 m^{-2} are adopted. The parameters of
 120 the BPMs and correctors are shown in Table 3.

121 C. RF errors

122 The errors of the RF system include the frequency, voltage
 123 and phase errors, which majorly comes from calibration, sys-
 124 tem shifting, closed orbit error and beam energy error of the
 125 storage ring, etc. The error information of the RF cavity can
 126 be obtained with beam transmission. The initial phase error
 127 of the RF cavity is usually large. The errors of the RF system
 128 are presented in Table 4.

129 D. Injection errors

130 As a 4th-generation light source, the HALF storage ring
 131 has a relatively large dynamic aperture, which greatly im-
 132 proves the ring acceptance and offers the possibility of us-
 133 ing the off-axis injection scheme. The injection system of the
 134 HALF storage ring adopts the pulsed nonlinear kicker (NLK)
 135 method [24, 25], which is simple in structure and has little
 136 disturbance to the stored beam. By using the pulsed NLK, the
 137 injected bunch is directly kicked into the phase space within
 138 the acceptance of the storage ring. The injected beam is then
 139 damped onto the closed orbit of the stored beam after sev-
 140 eral damping times. The stored beam, which goes through
 141 the central field-free region, has a little impact from the NLK,
 142 making the injection transparency for the light source users.

143 A full-energy linac with an energy of 2.2 GeV is used as
 144 the injector of the storage ring. The injected beam from the
 145 linac has an emittance of $500 \text{ pm} \cdot \text{rad}$. The NLK along with

146 a septum is located in one straight section, forming the whole
 147 injection system. The parameters of the injected beam at the
 148 injection position are shown in Tables 5, and the errors are
 149 described in Table 6.

150 IV. PERFORMANCE BEFORE CORRECTION

151 To figure out the difference between the ideal lattice and
 152 the actual one with errors, the performance of the HALF stor-
 153 age ring is studied before any correction. In a 4th-generation
 154 light source, the closed orbit (CO) may be absent without cor-
 155 rection. The existence of the CO is investigated by scaling
 156 the global error factor as depicted in Fig. 5. It shows that
 157 the CO exists when the scaling factor is less than 20%. As
 158 the factor increases to 100%, the existence possibility of the
 159 CO decreases to less than 20%. The deviation of the CO as a
 160 function of the global error factor is shown in Fig. 6. We can
 161 see that as the global error factor increases, the deviation in-
 162 creases until the closed orbit is lost. When the factor increases
 163 to a certain level, the orbit deviation reaches its maximum be-
 164 fore the beam is lost.

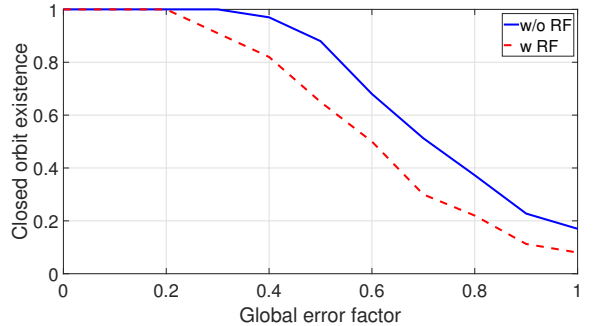


Fig. 5. (Color online) The closed orbit existence before any correction. The closed orbit exists when the scaling factor is less than 20%. As the factor increases to 100%, the existence possibility of the CO decreases to less than 20%.

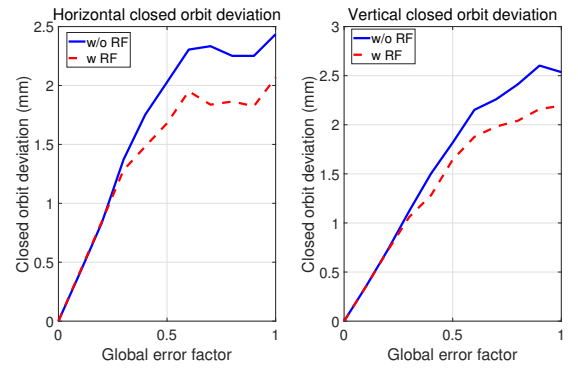


Fig. 6. (Color online) Deviation of the closed orbit as a function of the error scaling factor.

Table 2. Misalignment errors and field errors for the main magnets and girders. dx, dy, and ds represent the shift errors in the horizontal, vertical, and longitudinal plane respectively. rx, ry, and rs denote the rotation errors around the horizontal, vertical, and longitudinal axis respectively.

Element	dx(μm)	dy(μm)	ds(μm)	rx(μrad)	ry(μrad)	rs(μrad)	Field
Bends	200	200	150	200	200	100	5×10^{-4}
Quadrupoles	30	30	150	100	100	100	5×10^{-4}
Sextupoles	30	30	150	100	100	100	1×10^{-3}
Octupoles	30	30	150	100	100	100	1×10^{-3}
Girder	100	100	200	100	100	100	-

Table 3. Errors of the BPMs and corrector magnets.

Parameter	Value	Unit
BPM noise for TBT	1	μm
BPM noise for CO	0.1	μm
BPM calibration error	3	%
BPM offset	200	μm
BPM roll around s-axis	100	μrad
BPM gain	5	%
CM calibration error	5	%
CM strength limit	1	mrad
CM offset	200	μm
CM roll	200	μrad
Skew quadrupole strength limit	0.27	m^{-2}
Skew quadrupole calibration error	5×10^{-4}	-

Table 4. RF cavity errors.

Parameters	Values	Units
Voltage offset	1	%
Frequency offset	1×10^3	Hz
Time lag offset	90	Deg

Table 5. Parameters of the injected beam.

Parameters	Values	Units
ϵ_x/ϵ_y	500/500	$\text{pm} \cdot \text{rad}$
σ_x	58.18	μm
$\sigma_{x'}$	8.59	μrad
σ_y	35.70	μm
$\sigma_{y'}$	14.01	μrad
σ_δ	0.05	%
σ_ϕ	15	ps

Table 6. Errors of the injected beam.

Parameters	Systematic	Jitter	Units
Δx	100	10	μm
$\Delta x'$	100	10	μrad
Δy	100	1	μm
$\Delta y'$	100	1	μrad
$\Delta E/E$	5×10^{-4}	1×10^{-4}	-
$\Delta \phi$	0	0.1	Deg

165 V. SIMULATED COMMISSIONING FOR THE HALF 166 STORAGE RING

167 In this section, the correction chain of the simulated com-
168 misioning for the HALF storage ring is presented, which in-
169 cludes: A) Initial transmission correction (the first-turn tra-
170 jectory correction and second-turn trajectory correction), B)
171 Trajectory beam-based alignment, C) Injection correction, D)
172 Sextupole ramping, E) RF correction, F) Beam-based align-
173 ment and G) Optics correction. In order to avoid the influence
174 of the sextupoles and RF system on the beam dynamics, we
175 turn them off at the beginning of commissioning.

176 A. Initial transmission

177 The beam usually fails to form a closed orbit and even can
178 not pass through a complete turn in many cases at the be-
179 ginning of the ring commissioning. To obtain the first-turn
180 beam, the trajectory response matrix of the ideal lattice is
181 used to perform trajectory correction at the BPMs which have
182 turn-by-turn beam position signals. The correction process is
183 repeated to let more BPMs have position signals. If the iter-
184 ation yields no effect, the injected beam is scanned and the
185 kick strengths of the correctors before the failure position are
186 tuned until the beam passes through this BPM [26]. After
187 the first-turn trajectory correction, the particles are expected
188 to travel tens of turns. To further improve transmission of
189 the beam, the trajectory of the second turn is corrected to be
190 close to the first one. After the second-turn trajectory correc-
191 tion, more turns are expected to be achieved by the injected
192 particles. The cumulative distribution functions (CDFs) of
193 the beam loss under the first-turn and second-turn trajectory
194 corrections are shown in Fig. 7.

195 B. Trajectory beam-based alignment

196 Due to the magnetic field feed-down effect, the electron
197 beam would receive a kick when it travels away from the
198 center of the quadrupoles. This additional kick has a sig-
199 nificant impact on the beam transmission, especially for the
200 low-emittance storage rings adopting the quadrupoles with
201 strong strengths. To avoid this effect, the beam should pass
202 through the centers of all quadrupoles. The beam-based align-
203 ment (BBA) technique is used to determine the center of a

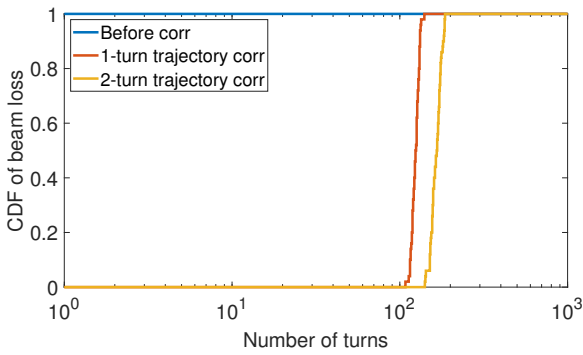


Fig. 7. (Color online) The cumulative distribution function of the beam loss after the first-turn and second-turn trajectory corrections.

quadrupole by using a nearby BPM and the orbit correctors. The beam position $\mathbf{X}(s_0)$ (trajectory or orbit) of the particles at the quadrupole position s_0 can be described by

$$\mathbf{X}(s_0) = x_0 \hat{\mathbf{x}} + y_0 \hat{\mathbf{y}}, \quad (1)$$

where x_0 and y_0 are particle offsets relative to the quadrupole magnet center in the horizontal and vertical plane respectively.

Due to the feed-down effect, this quadrupole can generate a dipole field,

$$B_x = B_0 \rho_0 K y_0, \quad (2)$$

$$B_y = B_0 \rho_0 K x_0, \quad (3)$$

where $B_0 \rho_0$ is the magnetic rigidity, K is the normalized quadrupole strength.

By changing the quadrupole strength with ΔK , the variation of the dipole field is given by

$$\Delta B_x = B_0 \rho_0 \Delta K y_0,$$

$$\Delta B_y = B_0 \rho_0 \Delta K x_0.$$

For the closed orbit scenario, this variation results in an orbit change at location s [27],

$$\Delta \mathbf{X}(s) = \Delta K \mathcal{T}(s, s_0) \mathbf{X}(s_0),$$

$$\begin{aligned} \mathcal{T}(s, s_0) = & \left(\frac{1}{1 - K_0 \frac{L_0 \beta(s_0)}{2 \tan(\pi\nu)}} \right) \\ & \times \frac{\sqrt{\beta(s)\beta(s_0)}}{2 \sin(\pi\nu)} \cos(|\phi(s) - \phi(s_0)| - \pi\nu), \end{aligned} \quad (7)$$

where L_0 is the length of the quadrupole, $\beta(s_0)$ and $\beta(s)$ are the beta functions at the location of the quadrupole and the observation point respectively. $\phi(s_0)$ and $\phi(s)$ are the betatron phases, and ν is the betatron tune.

The function $\mathcal{T}(s, s_0)$ is related with the Courant-Snyder (C-S) parameters, which can be considered as a constant

when the change of quadrupole strength ΔK is small. Then, the orbit change $\Delta \mathbf{X}(s)$ would be proportional to the orbit offset $\mathbf{X}(s)$. If the beam goes through the center of the quadrupole, the orbit change should theoretically be equal to zero. Using this principle, the quadrupole center can be obtained through measuring the orbit changes by varying the beam position in this quadrupole with a change in its strength ΔK [28]. If the beam orbit is least affected by changing the strength of the target quadrupole, the nearest BPM reading is considered as the center of the quadrupole.

The BBA process can also be applied to the trajectory case. The difference is that for the trajectory BBA, the beam position change is generated by adjusting the initial condition of the injected beam. After the trajectory BBA, the CDF of the beam loss is shown in Fig. 8, where an improvement in the beam transmission is seen.

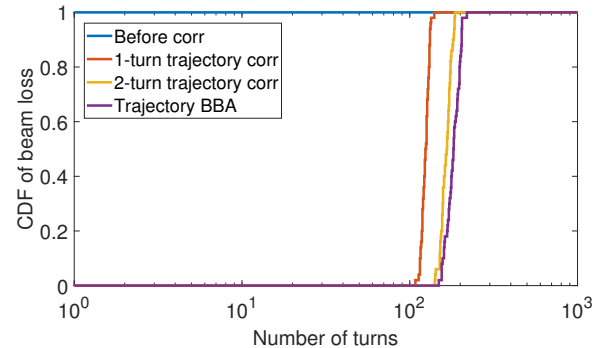


Fig. 8. (Color online) The cumulative distribution function of the beam loss after trajectory BBA.

C. Injection correction

To correct the static injection error, the injection correction is needed to obtain a better choice of the injection position.

In Fig. 9, the 1st-turn BPM readings in the upstream and 2nd-turn BPM readings in the downstream of injection position are (x_u, y_u) and (x_d, y_d) , where $x_{u,d}$ and $y_{u,d}$ are the BPM reading in the horizontal and vertical planes respectively. And the distances between the BPM and injection position are l_u and l_d . Then the injection point can be moved the position,

$$x_{\text{inj}} = l_d \frac{x_u - x_d}{l_u + l_d} + x_d, \quad (8)$$

$$y_{\text{inj}} = l_d \frac{y_u - y_d}{l_u + l_d} + y_d, \quad (9)$$

and the injection angle is given by

$$x'_{\text{inj}} = \frac{x_d - x_u}{l_u + l_d}, \quad (10)$$

$$y'_{\text{inj}} = \frac{y_d - y_u}{l_u + l_d}. \quad (11)$$

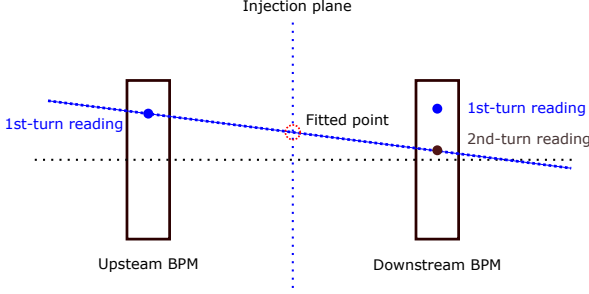


Fig. 9. (Color online) A schematic of the injection correction.

266 The CDF of the beam loss after the injection correction is
267 shown in Fig. 10.

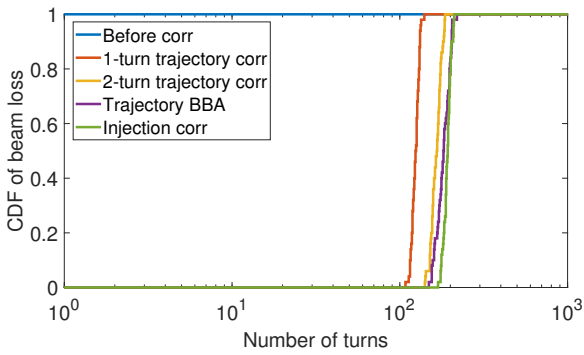


Fig. 10. (Color online) The cumulative distribution function of the beam loss after the injection correction.

268

D. Sextupole ramping

269 Due to the large nonlinear effect induced by the sextupoles,
270 we turn them off at the beginning of the commissioning. For
271 a storage ring, the chromatic sextupoles are needed to cor-
272 rect the chromaticities to positive values in order to avoid the
273 head-tail instability. Also the harmonic sextupoles are com-
274 monly adopted to optimize the dynamic performance of the
275 storage ring. For sextupole ramping, the strengths of all sex-
276 tupoles are increased in 5 steps. After each step, the trajectory
277 is corrected to the reference trajectory obtained from the tra-
278 jectory BBA. If necessary, the tune scan can be performed by
279 using two quadrupole families to improve the beam transmis-
280 sion. Until now the synchrotron radiation of all magnets are
281 on while the RF is turned off. The radiation loss per turn for a
282 single particle is 181.4 keV. The linear energy acceptance of
283 the HALF storage ring is 8.1%. This means the particles can
284 travel about 987 turns ideally. In Fig. 11, we can see that the
285 particles can go through near 600 turns, which shows an ef-
286 fective trajectory correction. Next we turn the RF on to form
287 the closed orbit.

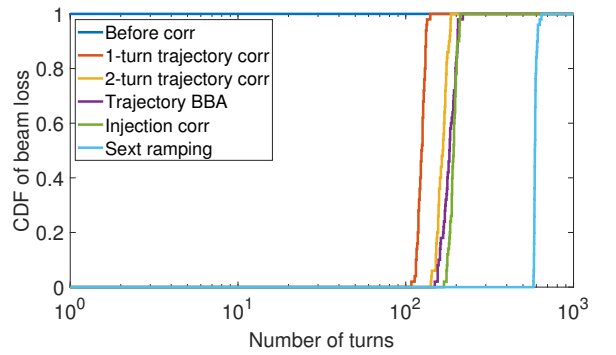


Fig. 11. (Color online) The cumulative distribution function of the beam loss after the sextupoles ramping.

288

E. RF correction

289 The BPM turn-by-turn (TBT) data can be used to correct
290 the phase and frequency errors of the RF system. Due to the
291 horizontal dispersion, the change of the horizontal beam po-
292 sition Δx induced by the energy variation ΔE is described
293 as [29]

$$294 \quad \frac{\Delta x}{\eta_x} = \frac{\Delta E}{E}, \quad (12)$$

295 where η_x is the horizontal dispersion, and E is the beam en-
296 ergy. The beam energy variation with the turn number n can
297 be expressed as [30, 31]:

$$298 \quad \Delta E_n = eV \sin(\Delta\omega T_0 n + \varphi_0 + \Delta\varphi) - U_0, \quad (13)$$

299 where V is the rf voltage, φ_0 is the synchronous phase, T_0 is
300 the synchronous period, U_0 is the radiation energy, $\Delta\omega$ and
301 $\Delta\varphi$ are the frequency and phase errors.

302 By integrating Eq. 13 over the turn number n and combin-
303 ing with Eq. 12, the beam energy change after n turns is given
304 by

$$305 \quad \frac{\Delta x}{\eta_x} = \frac{E_n - E_0}{E} = - \frac{eV}{\Delta\omega T_0 E} [\cos(\Delta\omega T_0 n + \varphi_0 + \Delta\varphi) \\ - \cos(\varphi_0 + \Delta\varphi)] - \frac{U_0 n}{E}. \quad (14)$$

306 Eq. 14 shows that the orbit variation is a function of the
307 frequency error $\Delta\omega$ and phase error $\Delta\varphi$. To correct the fre-
308 quency and phase errors, we can adjust $\Delta\omega$ and $\Delta\varphi$ to let Δx
309 be 0. To simplify this procedure, we can do this correction
310 separately.

311 For a real machine, the frequency error is usually small. To
312 correct the phase error firstly, we assume $\Delta\omega$ to be 0. Then
313 Eq. 14 turns out to be

$$314 \quad \frac{\langle \Delta x \rangle}{\eta_x} = \frac{\Delta x}{n\eta_x} \approx \frac{eV}{E} \sin(\varphi_0 + \Delta\varphi) - \frac{U_0}{E}, \quad (15)$$

315 which shows that the average horizontal beam position vari-
316 ation $\langle \Delta x \rangle$ is a sine function of the rf phase φ_0 . After three

317 iterations of the phase correction, the zero crossing is finally
 318 determined as the synchronous phase as shown in Fig. 12. To
 319 ensure at least 100 turns of beam transmission for the sub-
 320 sequent frequency correction, the tune scan is performed by
 321 changing the strengths of two quadrupole families after the
 322 first phase correction.

323 To correct the phase error $\Delta\phi$, $\Delta\omega T_0$ can be treated as a
 324 small quantity. Then Eq. 14 can be written as

$$325 \quad \frac{\langle \Delta x \rangle}{\eta_x} = \frac{\Delta x}{n\eta_x} \approx \frac{eV}{E} \left[\frac{1}{2} \Delta\omega T_0 n \cos(\varphi_0 + \Delta\varphi) \right. \\ \left. + \sin(\varphi_0 + \Delta\varphi) \right] - \frac{U_0}{E}, \quad (16)$$

326 where the average beam position variation $\langle \Delta x \rangle$ is a linear
 327 function of the frequency error $\Delta\omega$. A line is fitted and the
 328 zero crossing is considered as the synchronous frequency af-
 329 ter three iterations as shown in Fig. 13.

330 In the RF correction, the synchrotron motion should be
 331 taken into consideration. The number of the evaluated turns
 332 should be significantly smaller than 304 turns for the HALF
 333 storage ring, which is related to the synchrotron frequency
 334 of 2.06 kHz. Therefore, the average position of 20 turns are
 335 adopted. The CDF of the beam loss is shown in Fig. 14. The
 336 beam can pass through more than 1000 turns and finally be-
 337 comes a stored beam.

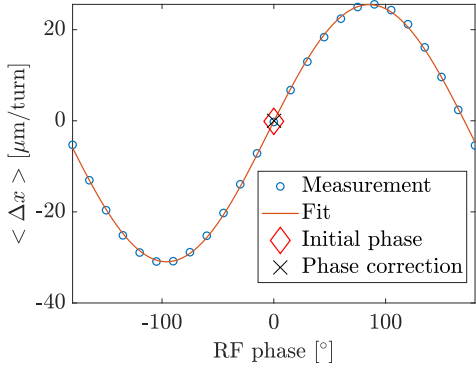


Fig. 12. (Color online) RF phase correction result in the final iteration.

F. Beam-based alignment

338 In this step, the closed orbit BBA is performed in order to
 339 obtain the golden orbit. The method used in the CO BBA is
 340 identical to the one mentioned in the previous subsection V B,
 341 except in the way of measuring the closed orbit. In the CO
 342 BBA, we use the orbit correctors to generate different kick
 343 strengths on the beam to move the beam inside the target
 344 quadrupoles. After performing the CO BBA, the closed orbit
 345 is corrected to the reference orbit. After the orbit correction,
 346 the strengths of all correctors with 10 sets of random error
 347 seeds are shown in Fig. 15. To mitigate the magnet feed-down
 348

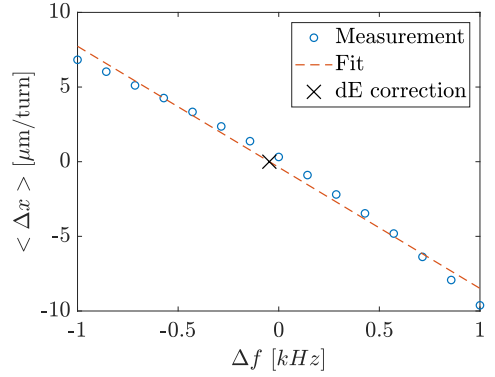


Fig. 13. (Color online) RF frequency correction result in the final iteration.

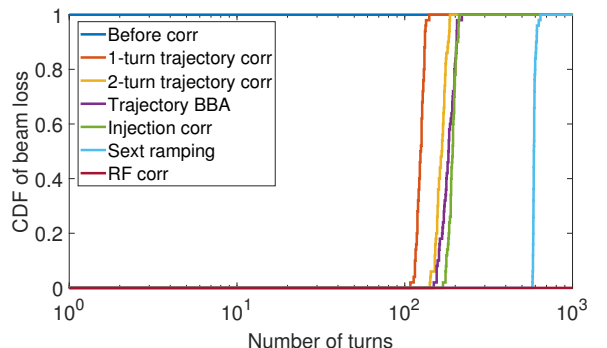
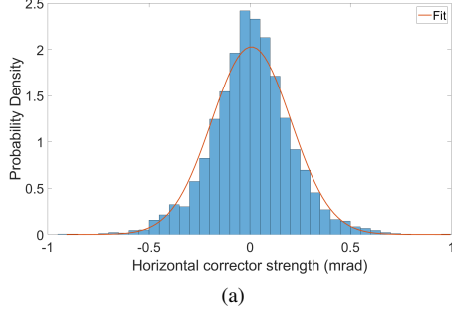


Fig. 14. (Color online) The cumulative distribution function of the beam loss after performing RF correction. The beam can be stored for more than 1000 turns.

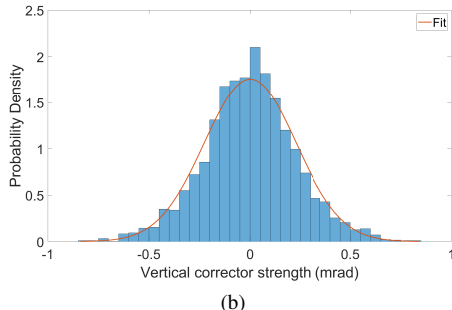
349 effect, moving the beam to the quadrupole centers is critical
 350 for the optics correction.

G. Optics correction

351 The linear optics is essential for the storage ring, which
 352 mainly includes the beta and dispersion functions. Due to
 353 the lattice errors, the optics would deviate from their ideal
 354 values, which can result in the shifts of the betatron tunes,
 355 reduction of the dynamic aperture, etc. To correct the linear
 356 optics, a commonly used technique called the LOCO (Lin-
 357 ear Optics from Closed Orbit) is performed, which can re-
 358 store the periodicity of the storage ring, decrease the negative
 359 effects of nonlinear resonances, and increase the beam life-
 360 time and DA [32, 33]. All quadrupoles are used for optics
 361 correction since they are powered independently. To correct
 362 the coupling, the skew quadrupole combined to the sextupole
 363 families SD1, SD2 and SF1 are used. The correction results
 364 for one error set are shown in Fig. 16 and Fig. 17. One can
 365 see that the beta beating and dispersion deviation is greatly re-
 366 duced to a low level. The periodicity of the lattice is restored
 367 as shown in Fig. 18. The betatron tunes are (0.193, 0.195),
 368 which are close to the ideal values (0.190, 0.190).

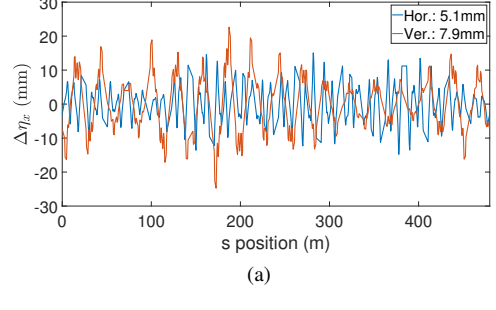


(a)

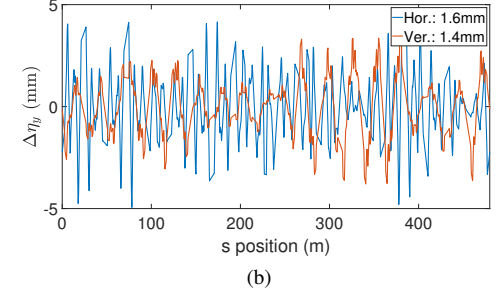


(b)

Fig. 15. Distribution of the corrector strengths after correcting the beam to the golden orbit: (a) Horizontal, (b) Vertical. The standard deviation of horizontal corrector strengths is 0.20 mrad, and the standard deviation of vertical corrector strengths is 0.23 mrad.

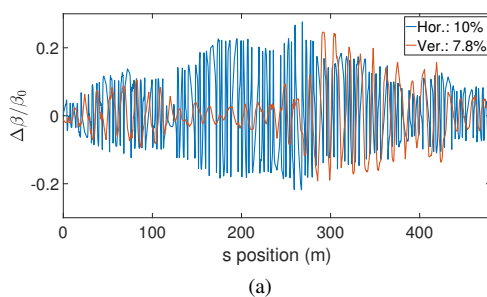


(a)

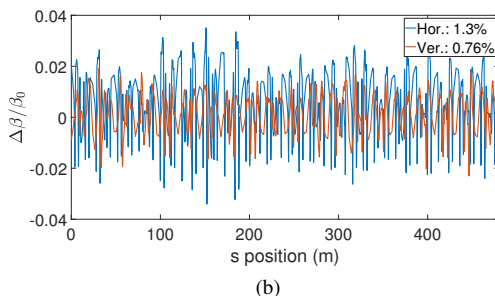


(b)

Fig. 17. Dispersion deviation of the HALF storage ring before and after optics correction: (a) Before correction, (b) After correction. The horizontal dispersion deviation (RMS) is reduced from 5.1 mm to 1.6 mm while the vertical dispersion deviation is reduced from 7.9 mm to 1.4 mm.

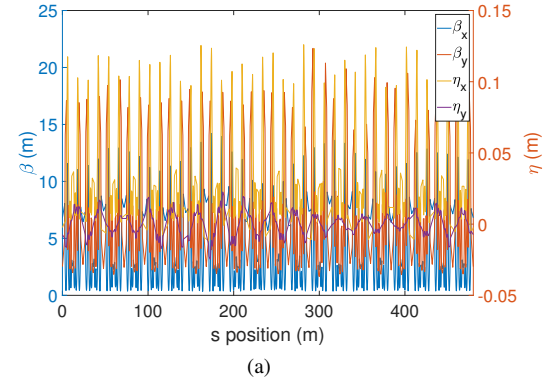


(a)

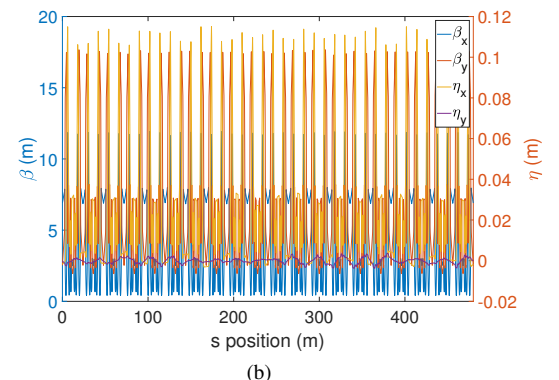


(b)

Fig. 16. Beta beating of the HALF storage ring before and after optics correction: (a) Before correction, (b) After correction. The horizontal beta beating (RMS) is reduced from 10% to 1.3% while the vertical beta beating is reduced from 7.8% to 0.76%.



(a)



(b)

Fig. 18. Linear optics of the HALF storage ring before and after correction: (a) Before correction, (b) After correction. It is obvious that the periodicity of the lattice is restored.

370

VI. SUMMARY AND CONCLUSION

The start-to-end commissioning simulation for the HALF storage ring is performed. For this 4th-generation light source ring, the electron beam can not form the closed orbit with errors at the beginning of the commissioning. After a series of effective correction procedures, the beam is stored, and the optic functions of the lattice are corrected to the ideal model. To figure out the recovery of the dynamic performance of the storage ring, the start-to-end commissioning simulation is performed with 10 sets of random error seeds. After the correction, the 6D dynamic aperture of the ring is close to the ideal one, as is seen in Fig. 19. It shows that the whole correction chain presented above is effective and successful. It guarantees a significant increase of our confidence in commissioning the real machine in the future. Also the commissioning software is going to be developed based on this sim-

ulated commissioning.

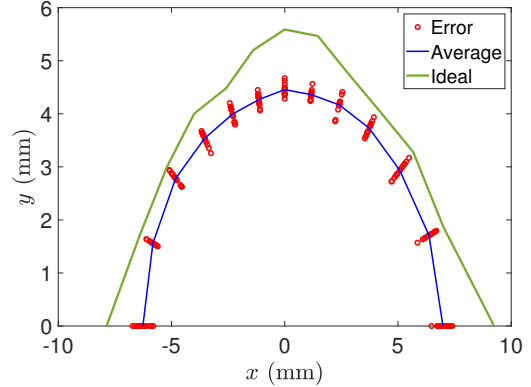


Fig. 19. (Color online) On-momentum 6D dynamic aperture of the HALF storage ring after correction.

387 [1] S. Mobilio, F. Boscherini, and C. Meneghini, *Synchrotron Ra- 425
388 diation: Basics, Methods and Applications* (Springer, 2015) pp. 1–799.
389
390 [2] K. Kim, *AIP Conference Proceedings* **184**, 565 (1989).
391
392 [3] Namkung and Won, in *Proceedings of IPAC’10, Kyoto, Japan* 426
393 (2010).
394
395 [4] D. H. Bilderback, P. Elleaume, and E. Weckert, *Journal of 427
396 Physics B: Atomic, Molecular and Optical Physics* **38**, S773 428
397 (2005).
398
399 [5] D. Einfeld, M. Plesko, and J. Schaper, *Journal of Synchrotron 429
400 Radiation* **21**, 856 (2014).
401
402 [6] M. Eriksson, J. F. van der Veen, and C. Quitmann, *Journal of 430
403 Synchrotron Radiation* **21**, 837 (2014).
404
405 [7] S. C. Leemann, S. Liu, A. Hexemer, M. A. Marcus, C. N. 431
406 Melton, H. Nishimura, and C. Sun, *Phys. Rev. Lett.* **123**, 432
407 194801 (2019).
408
409 [8] R. Hettel, *Journal of Synchrotron Radiation* **21**, 843 (2014).
410
411 [9] C. Steier *et al.*, in *Proceedings of IPAC’17*, International Par- 433
412 ticle Accelerator Conference No. 8 (JACoW, Geneva, Switzer- 434
413 land, 2017) pp. 2824–2826, <https://doi.org/10.18429/JACoW-IPAC2017-WEPAB104>.
414
415 [10] L. Liu, N. Milas, A. H. C. Mukai, X. R. Resende, and F. H. 435
416 de Sá, *Journal of Synchrotron Radiation* **21**, 904 (2014).
417
418 [11] J.C.Biasci, J.-F. Bouteille, N. Carmignani, J. Chavanne, 436
419 D. Coulon, Y. Dabin, F. Ewald, L. Farvacque, L. Goirand, 437
420 M.Hahn, J. Jacob, G.Lebec, S. M. Liuzzo, B. Nash, 438
421 H. Pedroso-Marques, T. Perron, E. Plouviez, P. Raimondi, J. L. 439
422 Revol, K. B. Scheidt, and V.Serrière, *Synchrotron Radiation 440
423 News* **27**, 12 (2014).
424
425 [12] M. Borland, T. Berenc, R. Lindberg, V. Sajaev, and 441
426 Y. Sun, in *Proceedings of North American Particle Acceler- 442
427 ator Conference (NAPAC’16), Chicago, IL, USA, October 9- 443
428 14, 2016*, North American Particle Accelerator Conference 444
429 No. 3 (JACoW, Geneva, Switzerland, 2017) pp. 877–880, 445
430 <https://doi.org/10.18429/JACoW-NAPAC2016-WEPOB01>.
431
432 [13] Y. Jiao, G. Xu, X. Cui, Z. Duan, Y. Guo, P. He, D. Ji, J. Li, X.- 446
433 Y. Li, C. Meng, Y. Peng, S. Tian, J. Wang, N. Wang, Y. Wei, 447
434 H.-S. Xu, F. Yan, C.-H. Yu, Y. Zhao, and Q. Qin, *Journal of 448
435 Synchrotron Radiation* **25**, 1611 (2018).
436
437 [14] Z. Bai, G. Feng, T. He, W. Li, W. Li, G. Liu, Z. Ren, 449
438 L. Wang, P. Yang, S. Zhang, and T. Zhang, in *Proceedings of 450
439 IPAC’21*, International Particle Accelerator Conference No. 12 451
440 (JACoW Publishing, Geneva, Switzerland, 2021) pp. 407–409, 452
441 <https://doi.org/10.18429/JACoW-IPAC2021-MOPAB112>.
442
443 [15] T. Hellert, P. Amstutz, C. Steier, and M. Venturini, *Phys. Rev. 453
444 Accel. Beams* **22**, 100702 (2019).
445
446 [16] H. C. et al., in *Proceedings of IPAC’23*, IPAC’23 - 14th Inter- 454
447 national Particle Accelerator Conference No. 14 (JACoW Pub- 455
448 lishing, Geneva, Switzerland, 2023) pp. 422–425.
449
450 [17] O. B.-G. et al., in *Proceedings of IPAC’23*, IPAC’23 - 14th Inter- 456
451 national Particle Accelerator Conference No. 14 (JACoW Pub- 457
452 lishing, Geneva, Switzerland, 2023) pp. 3263–3266.
453
454 [18] Z. M. et al., in *Proceedings of IPAC’23*, IPAC’23 - 14th Inter- 458
455 national Particle Accelerator Conference No. 14 (JACoW Pub- 459
456 lishing, Geneva, Switzerland, 2023) pp. 3104–3107.
460
461 [19] T. Hellert, I. Agapov, S. Antipov, R. Bartolini, R. Brinkmann, 462
462 Y.-C. Chae, D. Einfeld, M. Jebramcik, and J. Keil, in *Proced- 463
463 ings of IPAC’22*, International Particle Accelerator Conference 464
464 No. 13 (JACoW Publishing, Geneva, Switzerland, 2022) pp. 465
465 1442–1444.
466
467 [20] A. Terebilo, *Accelerator Toolbox for MATLAB*, Tech. Rep. 468
468 (SLAC National Accelerator Lab., Menlo Park, CA (United 469
469 States), 2001).
470
471 [21] A. Terebilo, in *Proceedings of the 2001 Particle Accelerator 472
472 Conference (PACS2001) (Cat. No.01CH37268)*, Vol. 4 (2001) 473
473 pp. 3203–3205 vol.4.
474
475 [22] Z. B. et al, *High Power Laser and Particle Beams* **34**, 104003 476
476 (2022).
477
478 [23] Z. B. et al., in *Proceedings of IPAC’23*, IPAC’23 - 14th Inter- 479
479 national Particle Accelerator Conference No. 14 (JACoW Pub- 480
480 lishing, Geneva, Switzerland, 2023) pp. 1075–1078.
481
482 [24] H. Takaki, N. Nakamura, Y. Kobayashi, K. Harada, T. Miya- 483
483 jima, A. Ueda, S. Nagahashi, M. Shimada, T. Obina, and 484
484 T. Honda, *Phys. Rev. ST Accel. Beams* **13**, 020705 (2010).
485
486 [25] G. Liu, W. Li, L. Wang, and P. Wang, in *Proceed- 487
487 ings of IPAC’21*, International Particle Accelerator Confer- 488
489 ence (IPAC’21), Geneva, Switzerland, 2021) pp. 489–491.

463 ence No. 12 (JACoW Publishing, Geneva, Switzerland, 2021) 474 [28] X. Huang, *Beam-based Correction and Optimization for Ac-*

464 pp. 2878–2880, [**22**, 040102 \(2019\).](https://doi.org/10.18429/JACoW-IPAC2021-475 celerators, 1st ed. (CRC Press, Boca Raton, 2019).</p>
<p>465 WEPAB119.</p>
<p>466 [26] S. Liuzzo, N. Carmignani, L. Farvacque, and B. Nash, 476 [29] S.-y. Lee, <i>Accelerator Physics Fourth Edition</i> (World Scientific</p>
<p>467 in <i>Proceedings of IPAC'17</i>, International Particle Accelerator Conference No. 8 (JACoW, Geneva, Switzerland, 2017) 477 Publishing Company, 2018).</p>
<p>468 pp. 3067–3070, <a href=)

469 WEPIK061.

470 [27] G. Portmann, D. Robin, and L. Schachinger, in *Proceedings of 479 [31] T. Hellert, C. Steier, and M. Venturini, Phys. Rev. Accel.*

471 Particle Accelerator Conference, Vol. 4 (1995) pp. 2693–2695 480 *Beams* **25**, 110701 (2022).

472 vol.4.

473 [32] J. Safranek, *Nuclear Instruments and Methods in Physics Research Section A: Accelerators, Spectrometers, Detectors and Associated Equipment* **388**, 27 (1997).

474 [33] G. J. Portmann, J. A. Safranek, and X. Huang, *MATLAB-481 BASED LOCO*, Tech. Rep. (SLAC National Accelerator Lab.,

475 Menlo Park, CA (United States), 2011).

476

477

478

479

480

481

482

483

484

485

486